Sonochemically synthesized ZnO and $Zn_{0.9}Cu_{0.1}O$ nanoparticles as photocatalysts for MB optodecolorization

M. KARIMI[a*], M. RASTEGAR RAMSHEH[a], A. JODAEI[b], S. M. AHMADI[c], V. JAHANGIR[d], M. GHASEMI[e], M. BEHTAJ LEJBINI[d]

[a]*Tracheal Diseases Research Center (TDRC), National Research Institute of Tuberculosis and Lung Diseases (NRITLD), Shahid Beheshti University of Medical Sciences, Tehran, Iran.*
[b]*Maham Tajhizat Parla Co., Chemistry & Chemical Engineering Research Center, Tehran, Iran.*
[c]*Department of Biomedical Engineering, Science and Research Branch, Islamic Azad University, Tehran, Iran.*
[d]*Department of Nanotechnology and Advanced Materials, Materials and Energy Research Center, Karaj, Iran.*
[e]*Department of Chemistry, Payame Noor University, Kermanshah, Iran.*

ZnO and $Zn_{0.9}Cu_{0.1}O$ nanoparticles were synthesized via sonochemical method using metal nitrate and urea precursors followed by calcination at temperatures of 300, 400 and 500 ˚C. The dependence of crystallite size, morphology, chemical purity, and optical properties of $Zn_{0.9}Cu_{0.1}O$ nanoparticles on calcination temperature was investigated by XRD, SEM, BET, EDS, FTIR and UV-vis absorption spectroscopy. XRD analysis showed the formation of hexagonal (nano)crystallites without any phase segregation upon doping Cu. The average crystallite size of $Zn_{0.9}Cu_{0.1}O$ nanoparticles showed an increase from 30 to 150 nm upon increase of calcination temperature from 300 to 500 ˚C. SEM micrographs revealed the synthesis of spherical particles, which underwent a grain growth upon increase of calcination temperature. BET measurements suggested the decrease of specific surface area of $Zn_{0.9}Cu_{0.1}O$ nanoparticles from 46.7 to 13.8 m^2/g with increase of calcination temperature from 300 to 500 ˚C. UV-vis absorption experiments showed the widening of the band gap of $Zn_{0.9}Cu_{0.1}O$ nanoparticles from 3.02 eV to 3.16 eV due to increase of calcination temperature. The photocatalytic activities of all synthesized materials toward methylene blue decolorization were also assessed. Based on the comparative results, the $Zn_{0.9}Cu_{0.1}O$ nanoparticles calcined at 300 ˚C show the best efficiency in methylene blue decolorization.

(Received April 19, 2016; accepted October 10, 2017)

Keywords: Nanoparticles, $Zn_{0.9}Cu_{0.1}O$, Sonochemical method, Photocatalytic decolorization

1. Introduction

Due to their high surface-to-volume ratio and superior optical, catalytic and electrical properties, metal oxide nanostructures have received a great interest for application in several areas. Zinc oxide semiconductor, with a wide direct band gap of 3.37 eV and a large exciton binding energy (60 eV), is one of the most promising metal oxides with numerous applications in gas sensors, catalysts, solar cells, field emission displays, pigments, etc. [1-5].

In recent years, many studies have been done on the photocatalytic treatment of environmental pollutants using ZnO nanomaterials [6-9]; however, due to some drawbacks of the photocatalysts based on ZnO nanomaterials, such as quick recombination of charge carriers, various studies are going on to improve the overall photocatalytic efficiency of ZnO nanostructures [9-11]. It appears that addition of specific impurities/dopants is a good method for optimization of optical, electrical and catalytic properties of ZnO nanostructures [12-21]. Recent works have shown that metal dopants are good choices for this purpose. Accordingly, different metal dopants such as In, Al, Mn, Fe, Cu, Ni, and rare earth elements such as Eu, Pr, and Ce have been employed for modifying the photocatalytic properties of ZnO nanostructures [12-21]. Since electronic, optical, and photocatalytic properties of semiconductor nanomaterials are significantly influenced by band gap engineering, copper (Cu) seems to be a good choice for modifying the catalytic properties of ZnO because of the small and direct band gap of CuO (1.85 eV) [22, 23]. Cu dopants could block the electron–hole recombination and subsequently scavenging electrons can reduce the recombination of charges enhancing the photocatalytic activity [21, 24, 25]. According to literature, the ideal Cu^{2+} concentration to obtain one-phase wurtzzite-like $Zn_xCu_{1-x}O$ is lower than 15% [26].

Among different methods for synthesis of doped and undoped ZnO nanostructures, the sonochemical method seems to be an advantageous method. Ease of operation, rapid processing, low processing cost and high efficiency of the sonochemical method has differentiated this method from other preparation methods such as, sol–gel, hydrothermal, solvothermal, co-precipitation, etc. The sonochemical method has been successfully used for the synthesis of nanoparticles and novel materials with unusual properties, including metals, alloys, metal oxides, chalcogenides, and metal nitrides [27-31]. This method has been also used for the synthesis of ZnO nanoparticles with various structures [4, 23, 32-34], and some metal

doped- ZnO nanostructures such as Fe-doped ZnO nanorods [19], and Ti (Sn)-doped single-crystalline ZnO nanorods [35]. The effect of ultrasonic energy in chemical reactions is not well understood; however, the results show that the extreme conditions (T>5000 K, P>1000 atm) resulted from implosive collapse of cavitation bubbles causes the formation of free radicals which in turns will lead to various chemical and physical effects. Furthermore, ultrasonic waves provide a violent mixing that accelerates the reaction rate. Therefore, nanostructured materials with various particle size, morphology, and purity can be synthesized under different sonochemical conditions such as sonication power, temperature, solvent, and concentration of reagents [36].

Synthesis of Cu-doped ZnO nanoparticles for photocatalytic applications has been reported by several researchers. Photoactive $Zn_{1-x}Cu_xO$ solid solutions ($0 \leq x \leq 0.1$) were synthesized by thermolysis of formate glycolate $Zn_{1x}Cu_x(HCOO)(OCH_2CH_2O)_{1/2}$ precursor at 500 ˚C and were used for hydroquinone oxidation [37]. Wu *et al.* prepared Cu-doped ZnO nanowires by a solvothermal route and examined their photocatalytic properties in degradation of azo dyes under visible light. The photocatalytic results indicated that doping of Cu into ZnO could enhance the photocatalytic efficiency of ZnO under visible light irradiation [38]. There is a study on investigation of photocatalytic activity of Cu-doped ZnO nanorods synthesized through the vapor transport method. The results of this study revealed the increased photocatalytic activity of Cu-doped ZnO nanorods compared to pure ZnO attributed to the intrinsic oxygen vacancies due to high surface to volume ratio in nanorods and extrinsic defect due to Cu doping [39]. Uhm *et al.* reported the synthesis of Fe- and Cu-doped ZnO nanorods by co-hydrolysis method for photomineralization of phenol. The obtained results showed the higher degradation of phenol in presence of Cu-doped ZnO nanoparticles [40]. Jacob *et al.* were used Cu doping to engineer the absorption spectrum of ZnO toward enhanced photocatalytic degradation of indigo carmine and orange G as anionic dyes, as well Rhodamine 6G and methylene blue as cationic dyes. The results confirmed that the presence of multivalent Cu on ZnO surface is responsible for the enhanced photoactivity [41].

To the best of our knowledge, there is only a report on synthesis of Cu-doped ZnO nanopowders by a two-step sonochemical method using metal nitrates and ammonia [42]. The present study is one of the first studies on investigating the photocatalytic activity of the sonochemially synthesized ZnO and $Zn_{0.9}Cu_{0.1}O$ nanoparticles. In addition, the method employed for synthesis of the ZnO based nanomaterials including

the type of precursors, precipitating-capping agent, dopant concentration, and heat treatment,

In this work, the effect of calcination temperature on structure, morphology and optical properties of $Zn_{0.9}Cu_{0.1}O$ nanoparticles were investigated and compared with those of pure ZnO nanoparticles. To study the photocatalytic properties of the synthesized nabomaterials, the photocatalysis tests were performed on methylene blue (MB) under various conditions.

2. Experimental

2.1. Materials

All the chemical reagents in our experiments were of analytical grade and purchased from Merck Company.

2.2. Synthesis of $Zn_{0.9}Cu_{0.1}O$ nanoparticles

$Zn_{0.9}Cu_{0.1}O$ nanoparticles was synthesized utilizing zinc nitrate hexa-hydrate ($Zn(NO_3)_2.6H_2O$), cupper nitrate tri-hydrate ($Cu(NO_3)_2.3H_2O$), and urea (CH_4N_2O) as a precipitating-capping agent to modify the surface of nanoparticles and prevent the growth of the particle to larger size. In a typical experimental procedure, 4.94 g of $Zn(NO_3)_2.6H_2O$ was dissolved in deionized water and 0.67 g of $Cu(NO_3)_2.3H_2O$ along with 3.25 g of urea was added to it, respectively. The solution was kept under stirring and heating (up to 70 ˚C) for 60 min and subsequently was transferred into an ultrasonic bath (40 kHz) where it was sonicated for 1 h. After sonication, the emerged precipitates were filtered and washed with ethanol and deionized water for several times to remove ionic impurities. The washed precipitates were dried at 60 ˚C for 10h and finally calcined at different temperatures of 300, 400 and 500 ˚C for 3 hours at a heating rate of 15 ˚C/min.

2.3. Synthesis of ZnO nanoparticles

The aforementioned method was applied for the synthesis of ZnO nanoparticles; in this case, only an aqueous solution saturated by 4.94 g zinc nitrate was used. The precipitated ZnO was calcined at temperature 300 ˚C for 3 hours.

2.4. Characterization of synthesized nanoparticles

The XRD patterns were recorded on a 3003TT Seifert using CuKα radiation (λ= 1.5406 Å). A LEO 7353 (1455 VP) scanning electron microscope (SEM) was used for morphological investigation of the nanoparticles. The elemental analysis of the products were performed by energy dispersive spectroscopy (EDS) using a Philips XL 30 instrument. The specific surface area of the synthesized powders was determined by nitrogen adsorption at 77 K using the BET (Brunauer–Emmett–Teller) method (BEL Japan, BELSORP-mini II). Fourier transform infra-red (FTIR) spectra of the powders were recorded using a Perkin-Elmer 100 instrument. The optical absorption of the nanoparticles were examined with a Perkin-Elmer 550 SE UV-vis spectrophotometer.

2.5. Photocatalytic testing

Photocatalytic tests were performed on methylene blue (MB) with various concentrations of 5, 10, 15 and 20 ppm at different temperatures of 25 (room temperature), 35, 45 and 55 ˚C. A high-pressure mercury UV lamp with a maximum emission of 365 nm and a fluorescent light lamp were used as UV and visible light sources, respectively. The decolorization of MB with ZnO and $Zn_{0.9}Cu_{0.1}O$ nanoparticles was carried out in a 200 ml beaker on a magnetic stirrer. 50 mg of the synthesized

nanoparticles and MB aqueous solution were loaded into the beaker to form a homogeneous suspension under stirring. The residual concentration of MB after each reaction was measured at the wavelength of 668 nm using the UV–vis spectrophotometer following removal of solid catalysts by centrifugation.

3. Results and discussion

3.1. Crystal phase characteristics

The X-ray diffraction patterns of ZnO and $Zn_{0.9}Cu_{0.1}O$ nanoparticles synthesized at different calcination temperatures are shown in Fig. 1. All the diffraction peaks for ZnO and $Zn_{0.9}Cu_{0.1}O$ nanoparticles are consistent with the ICDD file of ZnO (ICDD 76-0704), which can be indexed to hexagonal phase of ZnO. No peaks assignable to the possible impurities such as CuO indicates the synthesis of ZnO and $Zn_{0.9}Cu_{0.1}O$ nanoparticles with high phase purity [18-20, 43]. The lattice parameters for ZnO nanoparticles are calculated to be a = 0.3255 nm and c = 0.5214 nm. In addition, the lattice parameters of $Zn_{0.9}Cu_{0.1}O$ nanoparticles are estimated to be a = 0.3242 nm and c = 0.5205 nm. The smaller lattice parameters in $Zn_{0.9}Cu_{0.1}O$ nanoparticles can be ascribed to the substitution of the Cu ions (with a smaller ionic radius of 0.057 nm) relative to Zn (radius = 0.06 nm) sites without changing the crystal structure [44, 45].

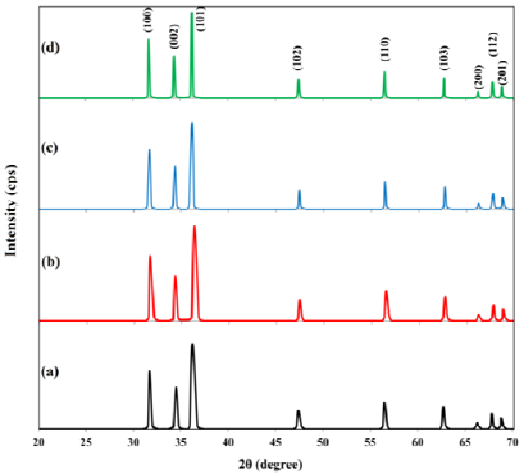

Fig. 1. XRD patterns of (a) ZnO nanoparticles; and $Zn_{0.9}Cu_{0.1}O$ nanoparticles obtained at (b) 300, (c) 400 and (d) 500 °C

For Cu-doped ZnO, no diffraction peaks related to Cu phases can be found in XRD patterns implying the uniform substitution of Cu^{2+} ions into the Zn^{2+} sites or interstitial sites in ZnO lattice. It is well known that the Cu^{2+} species migrate to the ZnO matrix and occupy lattice defects and disorders [41, 42]. This causes the formation of wurtzite (hexagonal)-like $Zn_xCu_{1-x}O$. According to the literature, only samples with copper content lower than 15% are one-phase wurtzite-like $Zn_xCu_{1-x}O$, while those with higher copper content contain a tenorite oxide phase [26]. The wurtzite structure is degraded gradually and CuO phase is also emerged with increasing the Cu concentration and occupation of defects [11]. There is a good agreement between our results and those reported in the literature.

The average crystallite size of ZnO and $Zn_{0.9}Cu_{0.1}O$ nanoparticles is determined from X-ray line broadening using Debye-Scherrer equation [46]:

$$d = \frac{0.94\,\lambda}{\beta cos\theta} \tag{1}$$

where d, λ, θ and β are the average crystallite size, X-ray wavelength (λ = 1.5406 Å), Bragg diffraction angle, and full width at half maximum (FWHM). From equation (1), the average crystallite size is found to be 40 nm for ZnO (calcined at 300 ˚C) and 30, 100 and 150 nm for $Zn_{0.9}Cu_{0.1}O$ nanoparticles calcined at 300, 400 and 500 ˚C, respectively.

Variation of the crystallite size with calcination time and temperature can be explained by normal crystal growth dynamics [11]:

$$D^n = D_0^n Kt \tag{2}$$

where D is the crystallite size at time t, D_0 the crystallite size at initial time t_0, n the dynamic growth index and K a constant. Provided that, α is the heating rate, then:

$$\alpha = \frac{dT}{dt} \tag{3}$$

where T is the absolute temperature at t. At the later period of the crystal growth, i.e., $D>>D_0$, the equation (2) can be changed into:

$$D^n = \frac{K}{\alpha}(T - T_0) \tag{4}$$

where T_0 is the temperature at t. By taking the logarithm, the equation (4) is reformed to following equation:

$$logD = \frac{K}{n\alpha} + \frac{log\,[T - T_0]}{n} \tag{5}$$

Fig. 2 shows the relation between $logD$ and $log[T\text{-}T_0]$. As expected from the equation (5), the figure reveals the direct relation between $logD$ and $log[T\text{-}T_0]$. The calculated dynamic growth index n from the slope of the straight line is to be 2.95. This indicates the quick growth of the $Zn_{0.9}Cu_{0.1}O$ nanoparticles during the heating process confirming the XRD results.

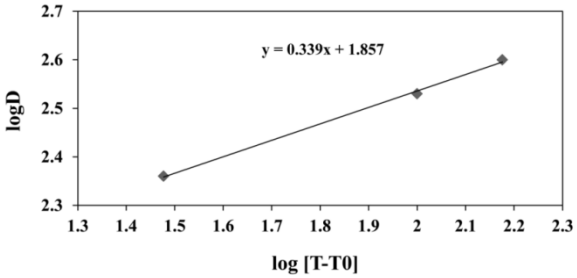

Fig. 2. Relation between logD and $log[T\text{-}T_0]$ for $Zn_{0.9}Cu_{0.1}O$ nanoparticle

3.2. Elemental analysis and morphology

Fig. 3 presents the EDS spectrum of Cu- doped ZnO nanoparticles. The spectrum shows that the nanoparticles are mainly composed of Zn and O, with some amount of Cu. Semi-quantitative analysis of EDS indicates that the atomic percentage (%) of Cu in Cu-doped ZnO nanoparticles is about 10%.

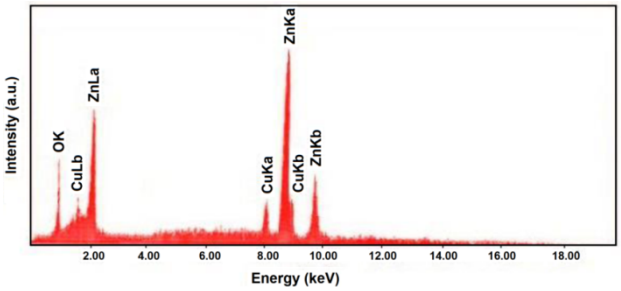

Fig. 3. EDS spectrum of $Zn_{0.9}Cu_{0.1}O$ nanoparticles

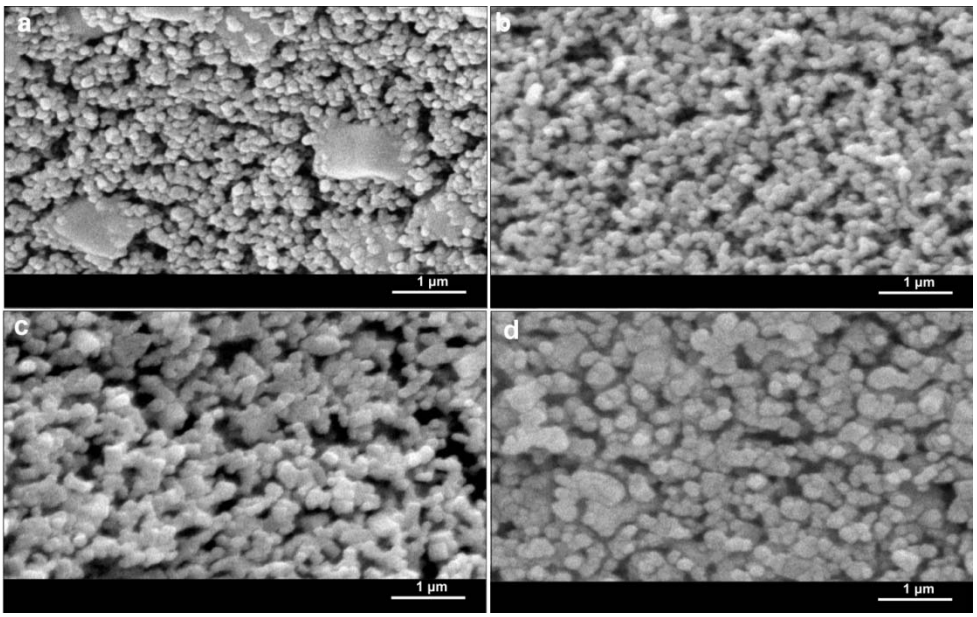

Fig. 4. SEM micrographs of (a) ZnO nanoparticles and $Zn_{0.9}Cu_{0.1}O$ nanoparticles obtained at (b) 300, (c) 400 and (d) 500 ˚C

Fig. 4 displays the SEM micrographs of the synthesized nanoparticles. It can be observed that the grain size of the spherical $Zn_{0.9}Cu_{0.1}O$ nanoparticles increases upon increase of calcination temperature from 300 to 500 ˚C.

3.3. BET surface area

Based upon BET data, the specific surface area of ZnO nanoparticles (calcined at 300 ˚C) and $Zn_{0.9}Cu_{0.1}O$ nanoparticles calcined at 300, 400 and 500 ˚C is measured to be 41.5, 46.7, 29.2, and 13.8 m^2/g, respectively. The average particle size of the nanoparticles is estimated from the BET surface area by assuming all the particles to have spherical shape. The average particle size (D_{BET}) in *nm* is calculated as [20]:

$$D_{BET} = \frac{6000}{S_{BET} \times \rho} \quad (6)$$

where S_{BET} is specific surface area in $m^2.g^{-1}$ and ρ is theoretical density of ZnO which is considered to be ~ 5.61 $g.cm^{-3}$. Accordingly, the average size of ZnO nanoparticles and Zn0.9Cu0.1O nanoparticles calcined at 300, 400 and 500 ˚C is calculated to be 25.8, 22.9, 36.62, and 77.5 nm, respectively.

3.4. Functional groups

Fig. 5 presents the FTIR spectra of $Zn_{0.9}Cu_{0.1}O$ nanoparticles obtained at different calcination temperatures. The broad absorption band at around 490 cm^{-1} is considered as stretching mode of Zn–O bond. The absorption bands located at 1387 and 1052 cm^{-1} are related to asymmetric and symmetric stretching modes of C=O groups in carbon dioxide molecules adsorbed onto the surface of nanoparticles during the synthesis process. The band sited at 2338 cm^{-1} is indexed to the bending vibrations of the intercalated O=C=O species produced by the urea decomposition in the initial process of preparation. The intensity of the latter band decreases upon increase of calcination temperature suggesting the further decomposition of urea molecules. The band at 1641 cm^{-1} along with a broad absorption peak at 3450 cm^{-1} are assigned to the O–H group in both adsorbed water molecules and as-formed metal hydroxides

($M(OH)_2$). The intensity of the aforementioned bands obviously decreases with increase of calcination temperature pertaining to the release of water molecules and further transformation of metal hydroxides into metal oxides [47-49].

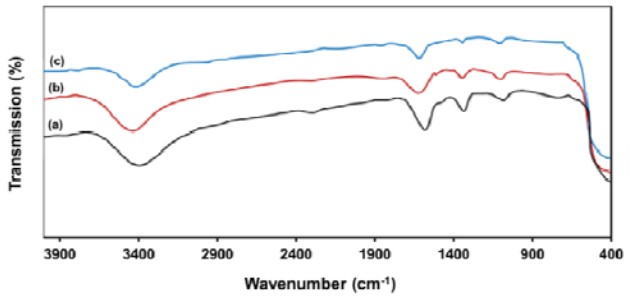

Fig. 5. FTIR spectra of $Zn_{0.9}Cu_{0.1}O$ nanoparticles obtained at (a) 300, (b) 400 and (c) 500 ˚C

3.5. Optical properties

The optical properties of ZnO and $Zn_{0.9}Cu_{0.1}O$ nanoparticles were examined by UV–vis absorption spectroscopy. The absorption spectra of ZnO and $Zn_{0.9}Cu_{0.1}O$ nanoparticles obtained at different temperatures are presented in Fig. 6. There can be observed a red-shift in the band edge of $Zn_{0.9}Cu_{0.1}O$ nanoparticles compared to pure ZnO nanoparticles which decreases upon increase of calcination temperature from 300 to ˚C.

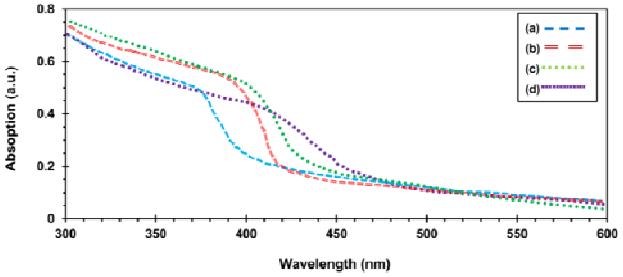

Fig. 6. UV–vis absorption spectra of (a) ZnO nanoparticles; and $Zn_{0.9}Cu_{0.1}O$ nanoparticles obtained at (b) 500, (c) 400 and (d) 300 ˚C

The band gap value of ZnO and $Zn_{0.9}Cu_{0.1}O$ nanoparticles is calculated from the optical absorption spectra using Tauc's relation [46]:

$$\alpha = \frac{A}{h\nu}(h\nu - Eg)^n \quad (7)$$

where, α is the absorption coefficient, $h\nu$ is the photon energy, A is a constant and n is equal to 1/2, 2, 3/2 and 3 for permitted direct, permitted indirect, forbidden direct and forbidden indirect transitions, respectively. For the permitted direct type of transitions, Tauc's relation is represented as [50]:

$$\alpha h\nu = A(h\nu - Eg)^{1/2} \quad (8)$$

Fig. 7 shows the variation of $(\alpha h\nu)^2$ versus $(h\nu)$ for the ZnO and $Zn_{0.9}Cu_{0.1}O$ nanoparticles. The optical band gap values are calculated by extrapolating the linear portion of the plots of $(\alpha h\nu)^2$ versus $h\nu$ to $\alpha = 0$. The direct band gap (E_g) values are found to be 3.31, 3.02, 3.1 and 3.16 eV for ZnO (calcined at 300 ˚C) and $Zn_{0.9}Cu_{0.1}O$ calcined at 300, 400 and 500 ˚C, respectively. Because of the direct band gap of CuO (1.85 eV), inclusion of Cu in ZnO leads to a red-shift in the band gap of $Zn_{0.9}Cu_{0.1}O$ nanoparticles compared to pure ZnO nanoparticles. Additionally, there is a slight shift in the band gap energies of $Zn_{0.9}Cu_{0.1}O$ nanoparticles with rising calcination temperature from 300 to 500 ˚C that can be attributed to the particle size effect in $Zn_{0.9}Cu_{0.1}O$ nanoparticles [51].

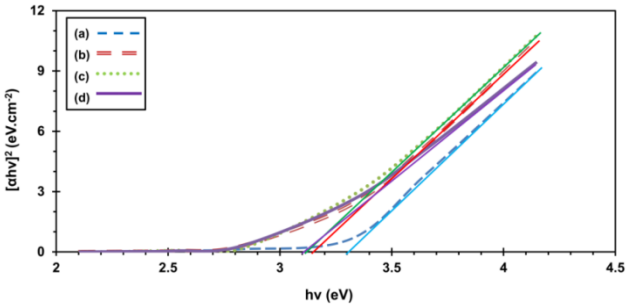

Fig. 7. Plot of $(\alpha h\nu)^2$ vs. $h\nu$ for determination of bandgap of (a) ZnO nanoparticles; and $Zn_{0.9}Cu_{0.1}O$ nanoparticles calcined at (b) 500, (c) 400 and (d) 300 ˚C

3.6. Photocatalytic activity of nanoparticles

Photocatalytic studies were performed on methylene blue (MB) in the wavelength of 668 nm (λ_{max}). Initially, experiments were carried out in the absence of the catalysts. There was no obvious decolorization of MB in absence of the catalysts under UV and visible light irradiation.

Photocatalytic decolorization of MB was investigated in the presence of four kinds of catalysts baesd on ZnO nanoparticles (designated as *nz*), $Zn_{0.9}Cu_{0.1}O$ nanoparticles calcined at 300 ˚C (designated as *nzc3*), $Zn_{0.9}Cu_{0.1}O$ nanoparticles calcined at 400 ˚C (designated as *nzc4*) and $Zn_{0.9}Cu_{0.1}O$ nanoparticles calcined at 500 ˚C (designated as *nzc5*) under UV and visible light irradiation. Figs. 8 and 9 show the variation of MB concentration in the form of lnC_0/C versus time (t). According to the figures, in all cases weather under UV or visible light irradiation, the photocatalytic activity of the catalysts is according to the following order:

$$nzc3 > nzc4 > nz > nzc5$$

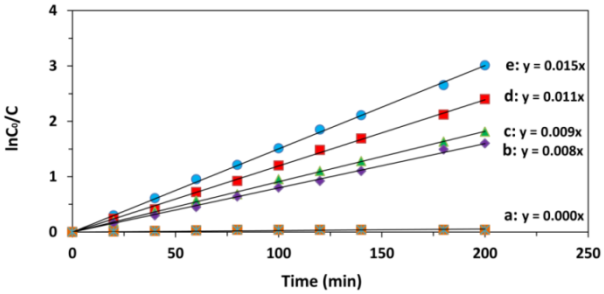

Fig. 8. UV light-induced photocatalytic decolorization of MB (20 ppm): (a) in absence of any catalyst, and in presence of (b) nzc5, (c) nz, (d) nzc4 and (e) nzc3 catalyst

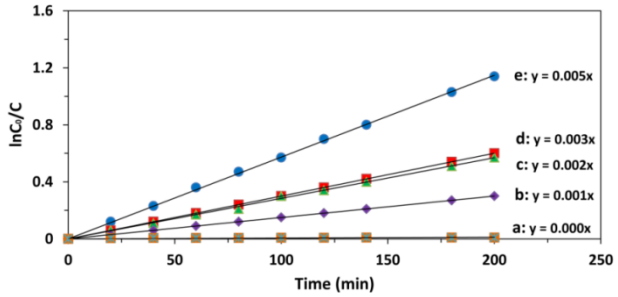

Fig. 9. Visible light-induced photocatalytic decolorization of MB (20 ppm): (a) in absence of any catalyst, and in presence of (b) nzc5, (c) nz, (d) nzc4 and (e) nzc3 catalyst

The differences in the photocatalytic activity of the catalysts can be assigned to the differences in the particle size, surface area, and band gap of the catalysts. The catalysts with smaller particle size (*nzc3* and *nz*) have higher oxygen vacancies, larger surface area and consequently, higher capability to absorb the light that in turn leads to further decolorization of MB. In addition, better photocatalytic activity of *nzc3* and *nzc4* compared with *nz* can be ascribed to the band gap engineering by Cu dopant that improves the electron trapping ability and inhibits electron–hole recombination. In this manner, the presence of transition metals such as Cu may increase the photocatalytic activity either by scavenging electrons that reduce the recombination of charges and therefore favors the $OH^{\bullet}$ formation, or by modifying the surface properties of the material including the active sites, defects, etc., which eventually increases the adsorption activity and favors the interfacial reactions [24, 25]. In the case of *nzc5* and *nz* catalysts, it seems that the effect of particle size is dominant (compared with dopant effect) leading to better photocatalytic activity of *nz* catalyst.

Figs. 10 and 11 show the effect of initial concentration of MB on photocatalytic activity of *nzc3* catalyst under UV and visible light irradiation. The figures reveal that the photocatalytic efficiency of the catalyst decreases with increasing MB concentration from 5 to 20 ppm; this can be concluded from decrease of the rate of photocatalytic reaction upon increase of MB initial concentration.

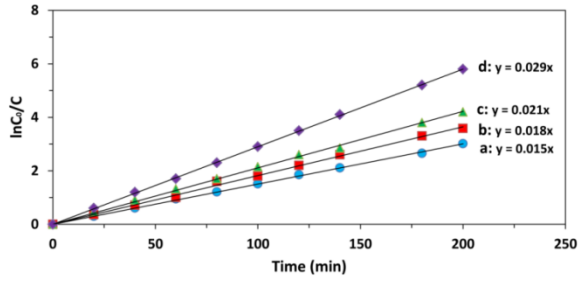

Fig. 10. UV light-induced photocatalytic decolorization of MB with initial concentration of (a) 20 ppm, (b) 15 ppm, (c) 10 ppm, and (d) 5 ppm by nzc3 catalyst at 25 ˚C

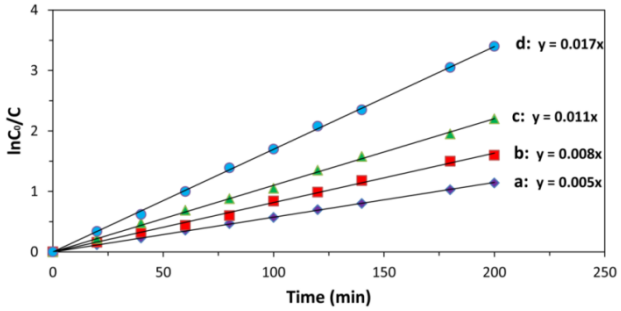

Fig. 11. Visible light-induced photocatalytic decolorization of MB with initial concentration of (a) 20 ppm, (b)15 ppm, (c)10 ppm, and (d) 5 ppm by nzc3 catalyst at 25 ˚C

Photocatalytic decolorization of MB by *nzc3* catalyst was also studied at various temperatures of 25, 35, 45 and 55 ˚C. Fig. 12 shows the plot of $ln(C_0/C)$ versus t at different reaction temperature. From the figure, the rate of photocatalytic degradation of MB increases upon increase of temperature. This is due to the increase of the collisions between MB molecules and catalyst that causes more contact with catalyst, and therefore, faster decolorization of the dye [43, 44]. Linear graphs observed in all figures confirm the pseudo-first-order-kinetics of MB decolorization reaction based on following equation:

$$ln\left(\frac{C_0}{C}\right) = k_{app} \times t \qquad (9)$$

where C_0 is the initial concentration value of the dye, C the concentration at time t and k_{app} is the apparent rate constant [52]. The obtained results including rate constant (k_{app}) and half-time ($t_{1/2}$) have been summarized in the Tables 1 and 2.

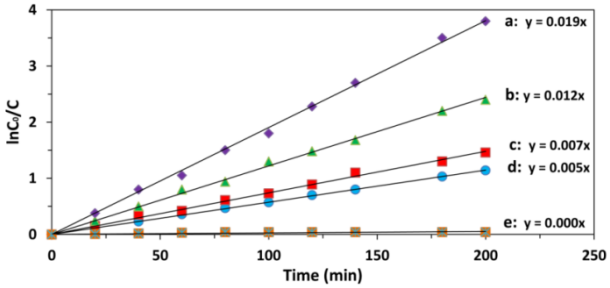

Fig. 12. Visible light-induced photocatalytic decolorization of MB (20 ppm) by nzc3 catalyst at temperature of (a) 55 ˚C, (b) 45 ˚C, (c) 35 ˚C, (d) 25 ˚C and (e) in absence of catalyst at 55 ˚C

Table 1. Apparent rate constant (k_{app}) and half-time ($t_{1/2}$) of photocatalytic decolorization of MB by various catalysts at different temperatures

catalyst	$k_{app}\times10^{-3}$ (min^{-1})					$t_{1/2}$ (min)				
	25˚C		35˚C (vis)	45˚C (vis)	55˚C (vis)	25˚C		35˚C (vis)	45˚C (vis)	55˚C (vis)
	UV	Vis.				UV	Vis.			
nz	9.0	2.0	-	-	-	77.0	346.5	-	-	-
nzc3	15.0	5.0	7.0	12.0	19.0	46.2	138.6	99.0	57.8	36.5
nzc4	11.0	3.0	-	-	-	63.0	231.0	-	-	-
nzc5	8.0	1.0	-	-	-	86.6	693.0	-	-	-

Table 2. Apparent rate constant (k_{app}) and half-time ($t_{1/2}$) of photocatalytic decoloration of MB with various concentration by nzc3 catalyst under UV and visible light irradiation

catalyst	$k_{app}\times10^{-3}$ (min^{-1}) at 25 ˚C				$t_{1/2}$ (min) at 25 ˚C			
	5 ppm	10 ppm	15 ppm	20 ppm	5 ppm	10 ppm	15 ppm	20ppm
***nzc3* + UV light**	29.0	21.0	18.0	15.0	23.9	33.0	38.5	46.2
***nzc3* + vis. light**	17.0	11.0	8.0	5.0	40.8	63.0	86.6	138.6

The photocatalytic activity of *nzc3* as the best photocatalyst in the study were compared with commercially available TiO_2 photocatalysts (Degussa P-25 and JRC-TiO_2) as reported in Ref. [21]. As described in Table 3, *nzc3* photocatalyst shows higher activity (in terms of photocatalytic rate constant) toward decoloration of MB (10 ppm) under UV light irradiation compared with both TiO_2-JRC and TiO_2-P25. The smaller particle size and engineered band gap of *nzc3* could be valid reasons for the enhanced photocatalytic activity. Accordingly, *nzc3* photocatalyst could be a suitable alternative to the best commercially available photocatalyst, i.e., TiO_2-P25 from both photocatalytic activity and affordability points of view.

Table 3. Performance of nzc3 photocatalyst compared to TiO_2-P25 and TiO_2-JRC in optodecolorization of MB

Photo-catalyst	Particle size (nm)	Band gap (eV)	Rate constant (min^{-1})	Ref.
nzc3	23 (from BET)	3.02	0.021	This work
TiO_2 (P25)	30-50	3.10	0.0133	[21]
TiO_2 (JRC)	20-50	3.20	0.0032	[21]

The apparent rate constant–temperature plot in the form of $-lnk_{app}$ versus temperature ($1/T$) is shown in Fig. 13. There is an Arrhenius-type relation between lnk_{app} and $1/T$ according to the following equation:

$$lnk_{app} = lnA - \frac{\Delta E}{RT} \qquad (10)$$

where, k_{app}, A, ΔE, R and T are the apparent rate constant, Arrhenius constant, activation energy, gas constant and temperature, respectively [43]. According to equation (10), the slope of the plot of lnk_{app} *vs.* $1/T$ gives the value of $\Delta E/R$ that can be used for calculating the activation energy. From the slope of the plot, the activation energy for photocatalytic reaction of MB is calculated to be 37.2 $kJ.mol^{-1}$. The low value of activation energy is another indication of the fast degradation of MB dye by *nzc3* catalyst.

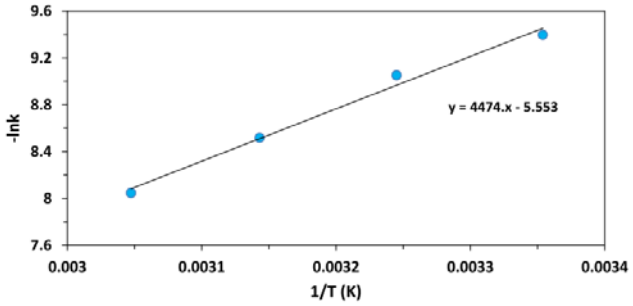

Fig. 13. Plot of $-lnk_{app}$ versus 1/T for visible light induced photocatalytic decolorization of MB by nzc3 catalyst

4. Conclusions

ZnO and $Zn_{0.9}Cu_{0.1}O$ nanoparticles were successfully synthesized by the sonochemical method in presence of metal nitrates ad urea. The effect of calcination temperature on crystal structure, particle size, morphology and optical properties of the nanoparticles was investigated by XRD, SEM, BET, EDS, FTIR techniques and UV-vis absorption spectroscopy. Based on the results, upon increase of calcination temperature from 300 to

500 ˚C, the average crystallite size of $Zn_{0.9}Cu_{0.1}O$ nanoparticles with wurtzite crystal phase increases from 30 to 150 nm, the purity of the nanoparticles gradually increases and their optical band gap increases from 3.02 to 3.16 eV. The dynamic growth index calculated for $Zn_{0.9}Cu_{0.1}O$ nanoparticles was found to be 2.95 that is an indicative of the quick growth of the $Zn_{0.9}Cu_{0.1}O$ nanoparticles during the calcination process. The photocatalytic degradation of MB in presence of the synthesized metal oxides confirmed the higher photocatalytic activity of $Zn_{0.9}Cu_{0.1}O$ nanoparticles calcined at 300 ˚C in comparison with other synthesized materials in this study. Apparent rate constant at room temperature and activation energy of the photocatalytic decolorization reaction of MB on $Zn_{0.9}Cu_{0.1}O$ nanoparticles (calcined at 300 ˚C) under visible light irradiation were estimated to be 0.005 min^{-1} and 37.2 $kJ.mol^{-1}$, respectively.

Acknowledgements

The authors would like to thank Masih Daneshvari Hospital, Shahid Beheshti University of Medical Sciences of Iran for the financial support.

References

[1] G. Applerot, N. Perkas, G. Amirian, O. Girshevitz, A. Gedanken, Appl. Surf. Sci. **256**, S3 (2009).
[2] M. Karimi, J. Saydi, M. Mahmoodi, J. Seidi, M. Ezzati, S. Shamsi Anari, B. Ghasemian, J. Phys. Chem. Solids **74**, 1392 (2013).
[3] X. T. Yin, W. X. Que, Y. L. Liao, J. Zhang, F. Y. Shen, Mater. Res. Innov. **16**, 213 (2012).
[4] B. G. Zhai, L. Yang, Y. M. Huang, Mater. Res. Innov. **19**, S15 (2015).
[5] J. Saydi, M. Karimi, M. Mazhdi, J. Seidi, F. Mazhdi, J. Mater. Eng. Perform. **23**, 3489 (2014).
[6] S. Li, Z. Ma, J. Zhang, Y. Wu, Y. Gong, Catal. Today **139**, 109 (2008).
[7] W. Wang, Z. Li, W. Zheng, H. Huang, C. Wang, J. Sun, Sens. Actuators B **143**, 754 (2010).
[8] M. Muruganandham, I. S. Chen, J. J. Wu, J. Hazard. Mater. **172**, 700 (2009).
[9] J. J. Wu, C. H. Tseng, Appl. Catal. B: Environ. **66**, 51 (2006).
[10] C. A. K. Gouvea, F. Wypych, S. G. Moraes, N. Duran, P. Peralta-Zamora, Chemosphere **40**, 427 (2000).
[11] G. Zhou, J. Deng, Mater. Sci. Semicond. Process. **10**, 90 (2007).
[12] A. Ishizumi, Y. Takahashi, A. Yamamoto, Y. Kanemitsu, Mater. Sci. Eng. B **146**, 212 (2008).
[13] S. Yun, J. Lee, J. Yang, S. Lim, Physica B **405**, 413 (2010).
[14] X. H. Lu, G. R. Li, W. X. Zhao, Y. X. Tong, Electrochim. Acta **53**, 5180 (2008).
[15] P. K. Sharma, R. K. Dutta, A. C. Pandey, J. Mag. Magn. Mater. **321**, 4001 (2009).
[16] Y. Zuo, S. Ge, Z. Chen, L. Zhang, X. Zhou, S. Yan, J. Alloys Compd. **470**, 47 (2009).
[17] T. H. Fang, S. H. Kang, Current Appl. Phys. **10**, 1076 (2010).
[18] D. Shuang, J. B. Wang, X. L. Zhong, H. L. Yan, Mater. Sci. Semicond. Process **10**, 97 (2007).
[19] E. Oh, S. H. Jung, K. H. Lee, S. H. Jeong, S. G. Yu, S. J. Rhee, Mater. Lett. **62**, 3456 (2008).
[20] K. Wei, W. Guo, C. Du, N. Zhao, X. Li, Mater. Lett. **63**, 1781 (2009).
[21] P. Pawinrat, O. Mekasuwandumrong, J. Panpranot, Catal. Commun. **10**, 1380 (2009).
[22] D. M. Fernandes, R. Silva, A. A. W. Hechenleitner, E. Radovanovic, M. A. Custódio Melo, E. A. G. Pineda, Mater. Chem. Phys. **115**, 110 (2009).
[23] M. Mazloumi, S. Zanganeh, A. Kajbafvala, P. Ghariniyat, S. Taghavi, A. Lak, M. Mohajerani, S. K. Sadrnezhaad, Ultrason. Sonochem. **16**, 11 (2009).
[24] M. Asilturk, F. Sayılkan, E. Arpac, J. Photochem. Photobio. A: Chem. **203**, 64 (2009).
[25] R. Ullah, J. Dutta, J. Hazard. Mater. **156**, 194 (2008).
[26] A. A. Khassin, V. V. Pelipenko, T. P. Minyukova, V. I. Zaikovskii, D. I. Kochubey, T. M. Yurieva, Catal. Today **112**, 143 (2006).
[27] T. Alammar, A. V. Mudring, Mater. Lett. **63**, 732 (2009).
[28] M. Barzegar, A. Habibi-Yangjeh, M. Behboudnia, J. Phys. Chem. Solids **70**, 1353 (2009).
[29] Q. Li, Y. Ding, M. Shao, J. Wu, G. Yu, Y. Qian, Mater. Res. Bull. **38**, 539 (2003).
[30] K. S. Suslick, T. Hyeon, M. Fang, J.T. Ries, A. A. Cichowlas, Mater. Sci. **225**, 903 (1996).
[31] Y. Koltypin, X. Cao, R. Prozorov, J. Balogh, D. Kaptas, A. Gedanken, J. Mater. Chem. **7**, 2453 (1997).
[32] S. Bhattacharyya, A. Gedanken, Micropor. Mesopor. Mater. **110**, 553 (2008).
[33] R. Wahab, S. G. Ansari, Y. S. Kim, H. K. Seo, H. S. Shin, Appl. Surf. Sci. **253**, 7622 (2007).
[34] X. Hou, F. Zhou, Y. Sun, W. Liu, Mater. Lett. **61**, 1789 (2007).
[35] L. Lv, D. Qian, X. Mo, Z. Cai, X. Xv, Z. Xv, Y. Dai, Mater. Res. Bull. **45**, 403 (2010).
[36] A. Esmaielzadeh Kandjani, M. Farzalipour Tabriz, B. Pourabbas, Mater. Res. Bull. **43**, 645 (2008).
[37] O. I. Gyrdasova, V. N. Krasilnikov, M. A. Melkozernova, E. V. Shalaeva, E. V. Zabolotskaya, L. Yu. Buldakova, M. Yu. Yanchenko, V. G. Bamburov, Proc. Rus. Acad. Sci. **447**, 288 (2012).
[38] C. Wu, L. Shen, H. Yu, Y. Zhang, Q. Huang, Mater. Lett. **74**, 236 (2012).
[39] R. Mohan, K. Krishnamoorthy, S. Kim, Solid State Comm. **152**, 375 (2012).
[40] Y. R. Uhm, B. S. Han, C. K. Rhee, S. J. Choi, J. Nanomater. **958586**, 1 (2013).

[41] N. M. Jacob, G. Madras, N. Kottam, T. Thomas, Ind. Eng. Chem. Res. **53**, 5895 (2014).
[42] D. Sahu, N. R. Panda, B. S. Acharya, A. K. Panda, Ceram. Int. **40**, 11041 (2014).
[43] D. Ayodhya, M. Venkatesham, A. S. Kumari, K. G. Mangatayaru, G. Veerabhadram, IOSR J. Appl. Chem. **6**, 1 (2013).
[44] R. Elilarassi, G. Chandrasekaran, J. Mater. Sci.: Mater. Electron. **21**, 1168 (2010).
[45] K. Milenova, I. Stambolova, V. Blaskov, A. Eliyas, S. Vassilev, M. Shipochka, J. Chem. Technol. Metall. **48**, 259 (2013).
[46] L. Xu, X. Li, J. Cryst. Growth **312**, 851 (2010).
[47] B. Wang, J. Iqbal, X. Shan, G. Huang, H. Fu, R. Yu, D. Yu, Mater. Chem. Phys. **113**, 103 (2009).
[48] Z. L. Liu, J. C. Deng, J. J. Deng, F. F. Li, Mater. Sci. Eng. B **150**, 99 (2008).
[49] D. Wu, M. Yang, Z. Huang, G. Yin, X. Liao, Y. Kang, X. Chen, H. Wang, J. Colloid Interface Sci. **330**, 380 (2009).
[50] J. Z. Kong, A. D. Li, H.F. Zhai, Y. P. Gong, H. Li, D. Wu, J. Solid State Chem. **182**, 2061 (2009).
[51] A. A. A. Ahmed, Z. A. Talib, M. Z. Hussein, A. Zakaria, J. Alloys Compd. **539**, 154 (2012).
[52] R. Albuquerque, M. C. Neves, M. H. Mendonc, T. Trindade, O. C. Monteiro, Colloids Surf. A: Physicochem. Eng. Aspects **328**, 107 (2008).

*Corresponding author: m.karimi@merc.ac.ir
karimi.merc@gmail.com